ACS NANO

University of Texas Libraries

Subscriber access provided by University of Texas Libraries

Article

Rational Design of a Ni3N0.85 Electrocatalyst to Accelerate Polysulfide Conversion in Lithium-Sulfur Batteries

Zihan Shen, Zili Zhang, Matthew Li, Yifei Yuan, Yue Zhao, Shuo Zhang, Chenglin Zhong, Jia Zhu, Jun Lu, and Huigang Zhang

ACS Nano, **Just Accepted Manuscript** • DOI: 10.1021/acsnano.9b09371 • Publication Date (Web): 28 May 2020

Downloaded from pubs.acs.org on May 29, 2020

Just Accepted

"Just Accepted" manuscripts have been peer-reviewed and accepted for publication. They are posted online prior to technical editing, formatting for publication and author proofing. The American Chemical Society provides "Just Accepted" as a service to the research community to expedite the dissemination of scientific material as soon as possible after acceptance. "Just Accepted" manuscripts appear in full in PDF format accompanied by an HTML abstract. "Just Accepted" manuscripts have been fully peer reviewed, but should not be considered the official version of record. They are citable by the Digital Object Identifier (DOI®). "Just Accepted" is an optional service offered to authors. Therefore, the "Just Accepted" Web site may not include all articles that will be published in the journal. After a manuscript is technically edited and formatted, it will be removed from the "Just Accepted" Web site and published as an ASAP article. Note that technical editing may introduce minor changes to the manuscript text and/or graphics which could affect content, and all legal disclaimers and ethical guidelines that apply to the journal pertain. ACS cannot be held responsible for errors or consequences arising from the use of information contained in these "Just Accepted" manuscripts.

is published by the American Chemical Society. 1155 Sixteenth Street N.W., Washington, DC 20036

Published by American Chemical Society. Copyright © American Chemical Society. However, no copyright claim is made to original U.S. Government works, or works produced by employees of any Commonwealth realm Crown government in the course of their duties.

Rational Design of a $Ni_3N_{0.85}$ Electrocatalyst to Accelerate Polysulfide Conversion in Lithium-Sulfur Batteries

Zihan Shen,† Zili Zhang,† Matthew Li,‡ Yifei Yuan,‡ Yue Zhao,† Shuo Zhang,† Chenglin Zhong,† Jia Zhu,†

Jun Lu,,‡ and Huigang Zhang*,†*

† National Laboratory of Solid State Microstructures, College of Engineering and Applied Sciences, and Collaborative Innovation Center of Advanced Microstructures, Nanjing University, Jiangsu, 210093, P.R. China

‡ Chemical Sciences and Engineering Division, Argonne National Laboratory, 9700 South Cass Avenue, Lemont, Illinois 60439, USA

E-mail: junlu@anl.gov, hgzhang@nju.edu.cn

ABSTRACT: Slow kinetics of polysulfides conversion reactions lead to severe issues for lithium-sulfur (Li-S) batteries, for example, low rate capability, polysulfides migration, and low Coulombic efficiencies. These challenges hinder the practical applications of Li-S batteries. In this study, we proposed a rational strategy of tuning the *d*-band of catalysts to accelerate the conversion of polysulfides. Nitrogen vacancies were engineered in hexagonal Ni_3N (space group $P6_322$) to tune its *d*-band center, leading to the strong interaction

between polysulfides and Ni_3N. Because of the more electron population onto the lowest occupied molecular orbital of Li_2S_4, the terminal S-S bonds were weakened for breaking. Temperature-dependent experiments confirm that $Ni_3N_{0.85}$ demonstrates much low activation energy, thereby accelerating the conversion of polysulfides. A Li-S cell using $Ni_3N_{0.85}$ can deliver a high initial discharge capacity of 1445.9 mAh g^{-1} (at 0.02 C) and low decay per cycle (0.039%). The $Ni_3N_{0.85}$ cell can also demonstrate an initial capacity of 1200.4 mAh g^{-1} for up to 100 cycles at a high loading of 5.2 mg cm^{-2}. The high efficiency of rationally-designed $Ni_3N_{0.85}$ demonstrates the effectiveness of the *d*-band tuning strategy to develop low-activation-energy catalysts and to promote the atomic understanding of polysulfides conversion in Li-S batteries.

KEYWORDS: nanocubes, lithium-sulfur batteries, $Ni_3N_{0.85}$, electrocatalyst, polysulfide conversion

Lithium-sulfur (Li-S) batteries attract increasing attention because of their high specific energy density (2600 W h kg^{-1}), low cost, environmental friendliness, and high abundance of sulfur resources.[1, 2] However, the practical applications of Li-S batteries are hindered by poor cyclability and low rate capability,[3-5] which originate from sluggish reaction kinetics, shuttle effects of polysulfides, volume changes, poor conductivities of sulfur species, multistep electron transfer, poor electrochemical properties of Li metal anodes, and so forth. Many strategies have been reported to accommodate the volume changes with porous structures,[6-8] to suppress polysulfide migration with adsorbents,[9] to improve electron transfer with the conductive network,[10-12] and to enhance the conversion of polysulfides with catalysts.[13-15] Among these strategies, the catalytic conversion of polysulfides not only enhances the kinetics of Li-S batteries during cycling but also increases the utilization ratio of sulfur species and relatively mitigates the polysulfides migration. Transition metal (TM)

catalysts (Pt,[16] Ni,[17] *etc.*) and their compounds (oxides,[7, 18-20] sulfides,[13, 21, 22] phosphides,[9, 23] carbides,[6, 24] nitrides,[25-27] *etc.*) have been extensively studied for catalyzing the conversion of polysulfides. However, catalytic effects were usually derived by observing the phenomenon of polysulfides adsorption and/or comparing the current responses of batteries using catalysts to those control samples without using catalysts. The properties enhancement was usually attributed to the strong adsorption between polysulfides and catalysts. Using such a typical approach, catalysts were developed by trial and error. The understanding of the catalytic mechanism is limited, especially at molecular or atomic levels.[28-31]

Polysulfide molecules (Li_2S_n, $4 \leq n \leq 8$) consist of S-S backbone and Li ions, which are mainly bonded through covalent and ionic interactions. A catalytic process must start from the adsorption. When a polysulfide molecule approaches the surface of a TM-based catalyst, Li ions may be attracted to under-coordinated non-metal anions and negatively-charged terminal S atoms are probably attached to metal cations on the exposed surface of catalysts. It is assumed that the frontier orbitals of polysulfide molecules mainly interact with *d*-orbitals of TM cations and *s, p*-orbitals of anions. Zhou *et al.* studied Co-based compounds on the catalytic process of Li-S batteries and found the *p*-band center modulates the interfacial electron transfer dynamics.[28] TM compounds usually have narrow *d*-bands of TMs over broad *p*-bands of non-metal anions. The *d*-band theory proposed by Norskov *et al.*[32] has received considerable success in the prediction of catalytic activities. However, it is unclear whether or not the modulation of *d*-bands works for Li-S batteries. If the *d*-bands of TMs compounds significantly affect polysulfide conversion, the *d*-bands engineering may allow rational design of Li-S battery catalysts, which is not available yet.

In addition, the catalytic effects were usually characterized by measuring the changes in rate capability or

current density of Li-S or symmetric cells, which vary dramatically with experimental conditions and sample preparation. It is urgently demanded to have a mechanistic method to characterize the intrinsic catalytic effect in Li-S batteries. According to transition state theory, reaction coordinate diagrams usually exhibit a saddle shape (Figure 1a). By studying a reaction at different temperatures, the free energy of activation can be found according to the Arrhenius equation. Low activation energy facilitates a fast reaction. Despite the wide applications of this relation in other fields, little is known about the activation energy of conversion reactions in Li-S batteries. More specifically, the information on how the surface atom alignment and defects affect the catalytic process is lacking, which prevents us from correlating the macroscopic properties to atomic structures and then devising the catalysts rationally.

Here, we developed a $Ni_3N_{0.85}$ electrocatalyst by engineering N vacancies in a hexagonal Ni_3N (space group $P6_322$), which was metallic and regarded as less active for catalytic conversion of polysulfides.[26] $Ni_3N_{0.85}$ interacts with Li_2S_4 strongly with the charge transfer from the surface to adsorbed Li_2S_4 molecules (Figure 1b) because of the rise of *d*-bands of Ni atoms. The strong interaction caused by N vacancies leads to the high filling fraction of the lowest occupied molecular orbital (LUMO) of Li_2S_4, thereby weakening the S-S bond of Li_2S_4 backbone and facilitating the bond breaking. Temperature-dependent experiments determine the activation energy of nucleation on $Ni_3N_{0.85}$ be only 8.11 kJ mol^{-1}, which is much lower than pristine Ni_3N (21.11 kJ mol^{-1}) and carbon (33.02 kJ mol^{-1}). Furthermore, we constructed hollow $Ni_3N_{0.85}$ nanocubes (Figure 1c) to host S species to suppress the polysulfide migration. Confining polysulfides in a porous host is a conventional method to suppress the polysulfide migration. The fabricated Li-S batteries are able to deliver a high initial discharge capacity of 1445.9 mAh g^{-1} at 0.02 C. A long-term cycling test shows that the Li-S battery lost only

0.039% of its initial capacity per cycle. Thanks to the efficient catalysis of $Ni_3N_{0.85}$ and confinements of hollow nanocubes, we are able to demonstrate Li-S batteries with a high loading of 5.2 mg cm^{-2} which shows an initial capacity of 1200.4 mAh g^{-1} for up to 100 cycles. In general, this study reports a high-efficiency $Ni_3N_{0.85}$ electrocatalyst for Li-S batteries and proposed the *d*-band tuning strategy to design low-barrier catalysts, which also promotes an in-depth understanding of polysulfide conversion at atomic levels.

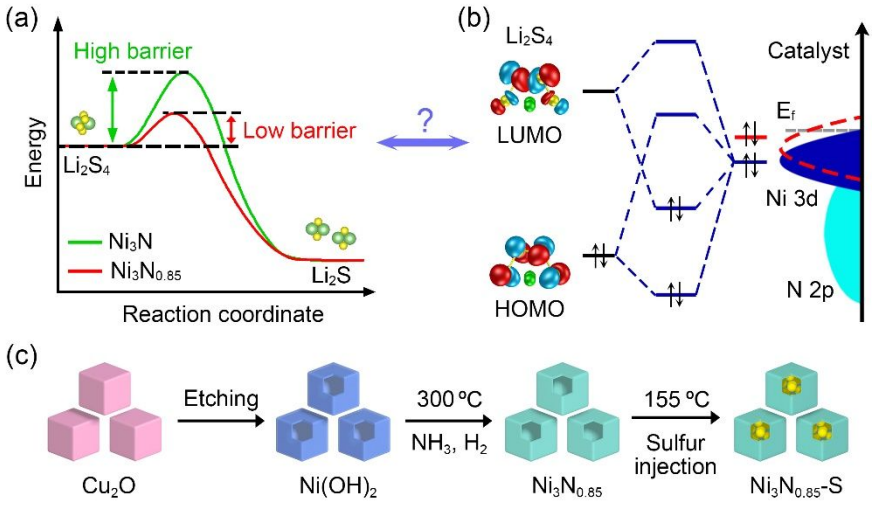

Figure 1. Schematic illustration of rational catalyst design by correlating (a) activation barrier with (b) orbital interactions between polysulfides and catalysts. Schematic diagram of the preparation procedures of Ni_3N_{1-x}–S cathodes.

RESULTS AND DISCUSSION

During the discharge of Li-S batteries, the solid-liquid conversion of Li_2S_4 to Li_2S plays an important role in battery properties because it accounts for 75% of the theoretical capacity. We studied the nucleation and growth of solid Li_2S on C (Super P), Ni_3N, and $Ni_3N_{0.85}$ using a potentiostatic technique (see Experimental section). Figure 2a-c show the current response curves when a constant voltage of 2.05 V is applied. The peaks in Figure 2a-c indicate the precipitation of Li_2S.[33] The integrated area below the current curves is related

to the nucleation capacity. A large capacity of 125.1 mAh g^{-1} indicates that Ni_3N can induce more nucleation of Li_2S than C (93.6 mAh g^{-1}). In contrast, $Ni_3N_{0.85}$ has the largest capacity of 145.5 mAh g^{-1} and the sharpest peak shape, implying rapid kinetics of polysulfides conversion on $Ni_3N_{0.85}$.

To decipher whether $Ni_3N_{0.85}$ is able to catalyze the polysulfide conversion, we measured the activation energies of the polysulfide conversion reactions by varying cycling temperatures for three typical samples (C, Ni_3N, and $Ni_3N_{0.85}$). Figure 2d-f show their cyclic voltammetric (CV) curves at three different temperatures (30, 40, and 50 °C). The anodic scan for the C cell exhibits a broad peak. In contrast, the Ni_3N and $Ni_3N_{0.85}$ cells show two split peaks, indicating that nickel nitride can accelerate the oxidation of polysulfides as compared to C. The cathodic scans of each cell show a minor peak around 2.31 V and a strong peak at 2.05 V, which correspond to the two plateaus of galvanostatic discharge curves. $Ni_3N_{0.85}$ has the smallest peak width at half-height, implying the most rapid kinetics. Given that the second peak contributes a large portion of capacity, we focused on the peak around 2.05 V to calculate the activation energy. The peak current (j) around 2.05 V is proportional to the reaction rates of Li_2S_4 to Li_2S, which can be fitted to Arrhenius equation ($j \propto A \times e^{-\frac{E_a}{RT}}$), where E_a is activation energy, R is gas constant, A is a pre-exponential factor, and T is temperature. Figure 2g presents the fitting lines for the three cells. In contrast to the high energy barriers for Ni_3N (21.11 kJ mol^{-1}) and C (33.02 kJ mol^{-1}), $Ni_3N_{0.85}$ has the lowest activation energy (8.11 kJ mol^{-1}) to catalyze the liquid/solid conversion. It is notable that the activation energy of $Ni_3N_{0.85}$ is 13 kJ mol^{-1} lower than that of Ni_3N, indicating that N vacancies significantly enhance the catalytic performance of Ni_3N. The catalytic effects can also be observed from the decreased polarization voltages (Figure 2h) or voltage gap between oxidative and reducing peaks. In addition, the $Ni_3N_{0.85}$ cell also shows a much lower Tafel slope (20 mV dec^{-1}) than those of C (208

mV dec^{-1}) and Ni_3N (68 mV dec^{-1}) cells (Figure 2i). The above analyses lead us to conclude that the decreasing activation energy from C, Ni_3N to $Ni_3N_{0.85}$ account for the increasing nucleation capacity in the chronoamperometric tests (Figure 2a-c).

To further understand how Ni_3N and $Ni_3N_{0.85}$ catalyze polysulfides conversion, we conducted a density functional theory (DFT) calculation. Figure 3a presents the crystallographic model of Ni_3N, which has an *hcp* arrangement of Ni with N in interstitial sites of Ni6 octahedra. The N occupation in octahedral sites expands the volume by 21% with respect to pure Ni. The electron density difference in Figure S1 (in the supplementary information (SI) shows that N vacancies transfer electrons mainly to their neighboring Ni, leading to the electron density changes of $Ni_3N_{0.85}$ as compared to untreated Ni_3N. A Bader charge analysis shows that the Ni around N vacancies gain about 0.23 electrons (Table S1). The partial density of state (PDOS) in Figure 3b shows that the Ni 3*d* bands cross the Fermi level, implying metallic conduction, which facilitates the charge transfer of electrocatalyst-assisted polysulfides conversion. It is noteworthy that after engineering N vacancies, the *d*-band center of $Ni_3N_{0.85}$ shifts towards the Fermi level (Figure 3b). A close inspection of geometry models indicates that the length of Ni-N bonds decreases whereas that of some Ni-Ni bonds increase (Figure S2). The lengthened Ni-Ni bonds lift the *d*-band center from −1.76 to −1.46 eV. According to the *d*-band theory, the upshift of *d*-band centers may cause strong interaction between adsorbed molecules and catalysts.[34, 35] Figure 3c and Table S2 shows the adsorption energies of three typical polysulfides (Li_2S_4, Li_2S_6, and Li_2S_8) on the $(1\bar{1}0)$ and $(1\bar{1}1)$ surfaces of Ni_3N and $Ni_3N_{0.85}$ (these two planes were chosen for modeling because they are most exposed, see models in Figure S3). In all cases of Figure 3c, vacancies-engineered $Ni_3N_{0.85}$ binds polysulfides more strongly than Ni_3N.

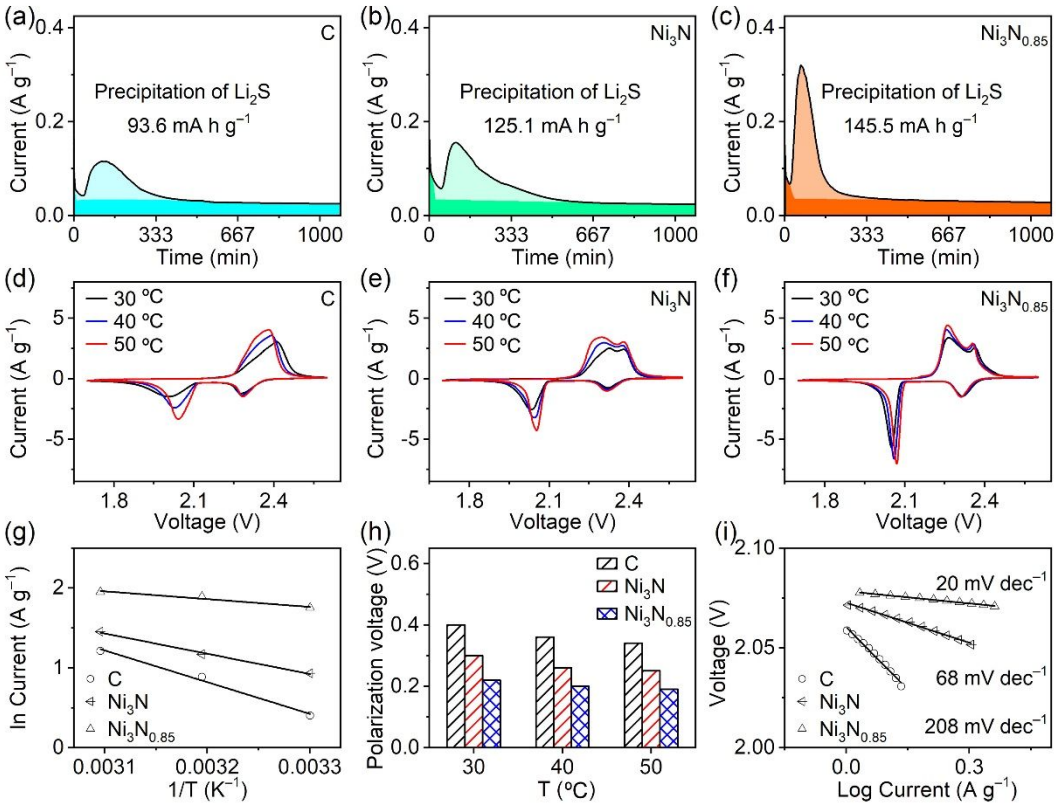

Figure 2. Electrochemical characterizations of electrocatalysts: (a–c) Chronoamperometric curves of nucleation tests using (a) C, (b) Ni_3N, and (c) $Ni_3N_{0.85}$ in a Li_2S_8/tetraglyme solution at 2.05 V (the regions with light and dark colors indicate the precipitation of Li_2S and the reduction of Li_2S_8/Li_2S_6, respectively). (d–f) CV curves of (d) C, (e) Ni_3N, and (f) $Ni_3N_{0.85}$ at different temperatures. (g) Relation of Li_2S_4 conversion rates with respect to temperatures in Li-S cells using C, Ni_3N, and $Ni_3N_{0.85}$. (h) Polarization voltage gaps of the reduction peaks around 2 V and their corresponding oxidation peaks. (i) Tafel plots for the CV curves between 2.03 and 2.08 V at 30 °C.

To gain more insight into interactions between polysulfides and nickel nitrides, we modeled the adsorption of Li_2S_4 on the $(1\bar{1}0)$ surface of Ni_3N and $Ni_3N_{0.85}$ and studied the changes of chemical bonds before and after Li_2S_4 adsorption. The optimized adsorption model in Figure 3d shows that each terminal S bonds to the bridge

site of two Ni atoms on the surface while two Li ions are attracted to two under-coordinated N atoms. The adsorbed Li_2S_4 molecule is stretched as compared to an isolated counterpart. Figure 3e presents the electron density difference of the adsorption of Li_2S_4 on the $(1\bar{1}0)$ surface of Ni_3N and $Ni_3N_{0.85}$ while Figure 3f is a slice of Figure 3e through the interacting Ni-S-Ni atoms. They show that N vacancies induce more electron density in the middle of Ni-S bonds, indicative of stronger covalence between terminal S and surface Ni atoms. To visualize the orbital and bonding, we calculated the maximally-localized Wannier orbitals (MLWO) of Li_2S_4 on $Ni_3N_{0.85}$. Figure 3g shows that the $3d_{xz}$ and $3d_{yz}$ orbitals of two bridge Ni atoms overlap with the $3p_x$ and $3p_z$ orbitals of the terminal S atoms, respectively (see the cartoon diagram of Figure 3g for the orbital interaction between S and Ni). A comparison with the molecular orbitals of isolated Li_2S_4 (Figure 1b) shows that the $3p_x$ and $3p_z$ MLWOs of terminal S may mainly comprise the highest occupied molecular orbital (HOMO) and LUMO of Li_2S_4, respectively. In view of the *d* orbitals of $Ni_3N_{0.85}$ being closer to the Fermi level than that of Ni_3N, the antibonding orbitals arising from both interactions may be emptied most probably, leading to the strong adsorption of Li_2S_4. To verify this reasoning, we conducted a visualized adsorption test. Ni_3N and $Ni_3N_{0.85}$ powder were added to an electrolyte solution containing polysulfides, respectively. The visualized adsorption of Li_2S_4 in Figure S4 shows that $Ni_3N_{0.85}$ is able to adsorb polysulfides and make electrolyte transparent more rapidly than both C and Ni_3N, confirming the strong interaction between Li_2S_4 and $Ni_3N_{0.85}$.

A strong interaction between bridged Ni atoms and terminal S causes more electrons to populate the LUMO of Li_2S_4 because of the upshift of the *d*-band center for $Ni_3N_{0.85}$, thereby weakening the S-S bonds. The crystal orbital overlap population (COOP) analysis in Figure 3h shows that the S-S bonds relative to terminal S atoms have more antibonding states below Fermi levels for $Ni_3N_{0.85}$ than that for Ni_3N. The changes in bonding states

agree with the stretched S-S bond length in Figure S5. These above analyses lead us to conclude that N vacancies-engineered $Ni_3N_{0.85}$ weakens the S-S bonds and facilitates the bond-breaking conversion of polysulfides, which explains the high catalytic performance and low activation energy of $Ni_3N_{0.85}$.

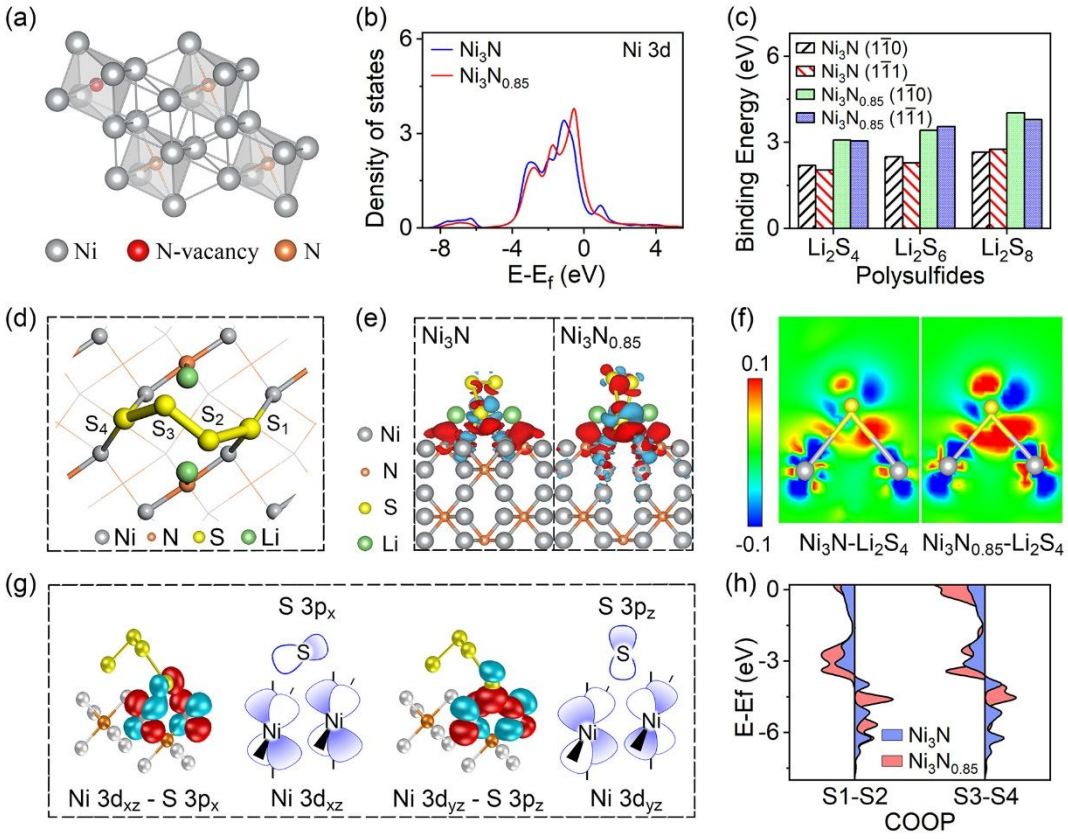

Figure 3. Theoretic analysis of the catalytic conversion of Li_2S_4: (a) Crystal structure of $Ni_3N_{0.85}$ for DFT calculations. (b) Partial density of states for Ni 3d orbitals of Ni_3N and $Ni_3N_{0.85}$. (c) Calculated binding energies between LiPSs (Li_2S_4, Li_2S_6, Li_2S_8) and catalysts (Ni_3N or $Ni_3N_{0.85}$). (d) Optimized configuration of Li_2S_4 on $Ni_3N_{0.85}$. (e) Electron density differences of Li_2S_4 on Ni_3N and $Ni_3N_{0.85}$ (the red and cyan regions represent negative and positive change the isovalue of ± 0.05). (f) Electron density differences in the slice planes through Ni-S-Ni bonds. (g) Interaction diagram of Wannier orbitals of Li_2S_4 on Ni_3N. (h) COOP diagram of the S1-S2 and S3-S4 bonds of Li_2S_4-absorbed Ni_3N and $Ni_3N_{0.85}$.

To use the catalyst for efficient polysulfides conversion, we first synthesized hollow $Ni_3N_{0.85}$ nanocubes to

confine sulfur species. Figure 4a shows the scanning electron microscope (SEM) image of $Ni_3N_{0.85}$ nanocubes, which were derived from cubic Cu_2O templates. The obtained nanocubes have a side length of ~70 nm and their morphology basically replicates that of the Cu_2O templates (Figure S6). A close observation on Figure 4a may allow one to discern holes on some $Ni_3N_{0.85}$ nanocubes. Most $Ni_3N_{0.85}$ nanocubes actually have continuous shells with hollow interiors (Figure 4b), which were formed by ion exchange and etch. Hollow interiors can host sulfur species and continuous shells may suppress polysulfide migration when used in S cathodes. These nanocubes have a high surface area of 56.6 $m^2 g^{-1}$ (Figure S7), which facilitates the catalytic conversion of polysulfides. The selected area electron diffraction (SAED) pattern in the inset of Figure 4b shows multiple rings, which are in agreement with those of polycrystalline Ni_3N (JCPDS card #10-0280). The scanning transmission electron microscope (STEM) image in Figure 4c reveals dark cores in nanocubes, confirming the formation of hollow structures. The energy-dispersive X-ray spectroscopy (EDX) mapping images in Figure 4c show that elemental N has a similar distribution as Ni. After loading with S, $Ni_3N_{0.85}$ retains its cubic morphology as shown in Figure 4d. The transmission electron microscope (TEM) analysis in Figure 4e and Figure S8 indicate that S was mainly loaded into the interiors of $Ni_3N_{0.85}$. The core region of the nanocube in the STEM image of Figure 4f is brighter than that of Figure 4c because the loaded S increase the electron scattering. The EDX mapping images in Figure 4f confirm the uniform distribution of S elements inside the core of nanocubes (see a EDX line scan in Figure S9 for more evidence). The X-ray diffraction (XRD) pattern of nanocubes generally matches that of Ni_3N (JCPDS card #10-0280). The zoomed-in inset in Figure 4g indicates that after treatment with forming gas (Ar/H_2), the (111) peak of $Ni_3N_{0.85}$ shifts to a higher angle than that of untreated Ni_3N, implying the shrunk lattice parameters. The peak intensity in Figure 4g

decreases and the width increases, mainly owing to the formation of vacancies. The significant intensity of XRD peaks relative to S confirms that S was loaded onto nanocubes and seems inert with $Ni_3N_{0.85}$. The inductively coupled plasma-optical emission spectrometry was sued to quantify the chemical composition of $Ni_3N_{0.85}$, confirming the formation of N vacancies. The above characterizations demonstrate that using a template conversion technology, we successfully synthesized $Ni_3N_{0.85}$ nanocubes having high surface area, hollow interiors, and continuous shells, which render vacancies-engineered nanocubes suitable to host S for Li-S battery cathodes.

X-ray photoelectron spectroscopy (XPS) was conducted for $Ni_3N_{0.85}$ and Li_2S_4-absorbed $Ni_3N_{0.85}$ (labeled as $Ni_3N_{0.85}$–Li_2S_4), as well as untreated Ni_3N for comparison. The Ni 2*p* signals in Figure 4h consist of two main peaks due to spin-orbit splitting and their satellites. Each main peak can be deconvoluted into two components originating from Ni^{2+} and Ni^{+} ions. The Ni^{2+} signals at 856.1 and 873.9 eV are ascribed to surface oxides.[36] After engineering N vacancies, the Ni^{+} components shift to lower energies, indicating the reduction of Ni probably because N vacancies transfer electrons to neighboring Ni atoms.[37] The N 1*s* peak at 397.8 eV is associated with the binding energy of Ni-N (Figure 4i).[38] After treatment in forming gas, a weak peak appears at 400.0 eV, which can be attributed to N-O species formed by surface oxidation according to previous reports.[39, 40] After absorbing Li_2S_4, the Ni^{+} peaks of $Ni_3N_{0.85}$–Li_2S_4 shift toward higher energies than pristine $Ni_3N_{0.85}$, indicating the electron transfer from $Ni_3N_{0.85}$ to Li_2S_4. Figure S10 further confirms the electron redistribution to S because of the shift of S 2p peaks to lower binding energy.[8, 41-43]

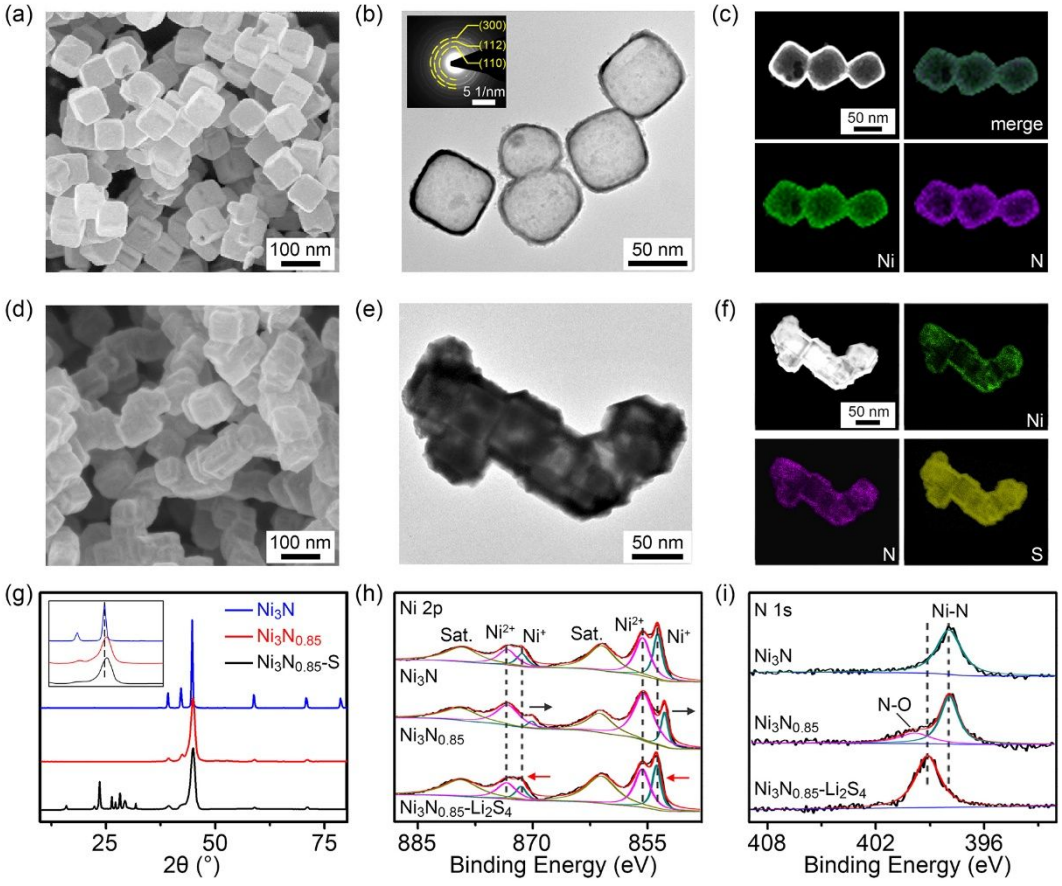

Figure 4. Materials characterizations of electrocatalysts: (a) SEM and (b) TEM images of as-prepared $Ni_3N_{0.85}$ nanocubes (the inset in (b) is the SAED pattern of nanocube). (c) STEM image and EDX mapping images of elemental Ni and N in $Ni_3N_{0.85}$ nanocubes. (d) SEM, (e) TEM, and (f) EDX elemental mapping images of $Ni_3N_{0.85}$–S nanocubes. (g) XRD patterns of Ni_3N, $Ni_3N_{0.85}$, and $Ni_3N_{.085}$–S (the inset shows the zoomed region of (111) peaks). XPS spectra of (h) Ni 2p and (i) N 1s for Ni_3N, $Ni_3N_{0.85}$, and $Ni_3N_{0.85}$–Li_2S_4.

Figure 5a shows the galvanostatic charge/discharge curves of three typical Li-S cells using $Ni_3N_{0.85}$, Ni_3N, and C cathodes. The $Ni_3N_{0.85}$ cell delivers a discharge capacity of 1445.9 mAh g^{-1} and a Coulombic efficiency (CE) of 94.6%, which are much higher than those of the Ni_3N (1300.9 mAh g^{-1}, 91.3%) and C (972.8 mAh g^{-1}, 85.1%) cells. More notably, the voltage gap of the $Ni_3N_{0.85}$ cell at half capacity is only 0.12 V, which is the lowest among the three cells, indicating that the catalytic activity of $Ni_3N_{0.85}$ decreases the kinetic resistances

of Li-S batteries. Many studies[10, 31] employed symmetric cells (Figure 5b) to qualitatively test whether or not the catalytic effect of polysulfide conversion exists. To verify the effective polysulfide catalysis that we derived from activation energy measurements and atomic modelling, the method of symmetric cells was also applied to three pair of identical electrodes of $Ni_3N_{0.85}$, Ni_3N, and C. As shown in Figure 5c, the considerably large current response for $Ni_3N_{0.85}$ contrast the nearly zero current for C, further confirming the catalytic effect of $Ni_3N_{0.85}$ for the conversion of Li_2S_4 in the electrolyte.

Figure 5d shows the rate capability of three cells with the S loading of 1.5 mg cm^{-2}. When the C rate increases from 0.1 C to 4 C, the capacity of the $Ni_3N_{0.85}$ cell decreases from 1267.6 to 590.6 mAh g^{-1}. As compared to $Ni_3N_{0.85}$, the Ni_3N and C cells have low capacity at varied C rates and lose more capacities at high C-rates. To compare the cyclability of the three cells, a galvanostatic cycling test is conducted and shown in Figure 5e. At 0.1 C, the $Ni_3N_{0.85}$ cell delivers an initial capacity of 1227.9 mAh g^{-1}, which drops gradually to 972.8 mAh g^{-1} in 100 cycles and maintains a low decaying rate of 2.6 mAh g^{-1} per cycle. In contrast, the Ni_3N and C cells lose almost 51.4% and 34.5% of their initial capacities, respectively. The CV curves of the cycled cells (Figure S11) clearly indicates that the $Ni_3N_{0.85}$ cell retains high capacity. Figure 5f present the electrochemical impedance spectra (EIS) at 1.7 V after 10 cycles between 100 kHz and 10 mHz (The EIS of fresh cell is shown in Figure S12 for comparison). The high-frequency intercepts for three cells are similar, indicative of a well-controlled comparison. A shorter semicircle diameter for the $Ni_3N_{0.85}$ cell than C and Ni_3N indicates the fast charge transfer, which is attributed to the high catalytic activity of $Ni_3N_{0.85}$. Thus, it is inferred that the high capacity retention in galvanostatic cycling results at least partly from the highly efficient catalysis enabled by vacancies. The Ni_3N cell exhibits relatively higher capacity retention than the C cell. By comparing

their morphology (Figure S13), one may derive that the hollow interior and continuous shell of nanocubes help to confine the sulfur species. The confinement effect stands out when the S loading increases to 5.2 mg cm^{-2} as shown in Figure 5g. Because of the lack of nanocubes confinement, the C cell at high S loading loses capacity rapidly. The effective confinement and catalysis render the $Ni_3N_{0.85}$ cell cycling steadily with a low decaying rate of 3.7 mAh g^{-1} per cycle. Figure 5h presents the long term cycling properties of a $Ni_3N_{0.85}$ cell (1.5 mg cm^{-2}) at 2 C. Its CE rapidly increases from 82.9% in the first cycle to 99.0% in the 20th cycle. Even after 1000 cycles, it retains a capacity of 669.4 mAh g^{-1}, indicative of a low decaying rate of only 0.039% per cycle on average. After cycling, $Ni_3N_{0.85}$ nanocubes retain their morphology and crystal structure as shown in Figure S14, indicating good stability. As compared to other previously-reported metal nitrides (Table S3) and nanostructured catalysts (Table S4), $Ni_3N_{0.85}$ is able to significantly improve the cyclability of S cathodes.

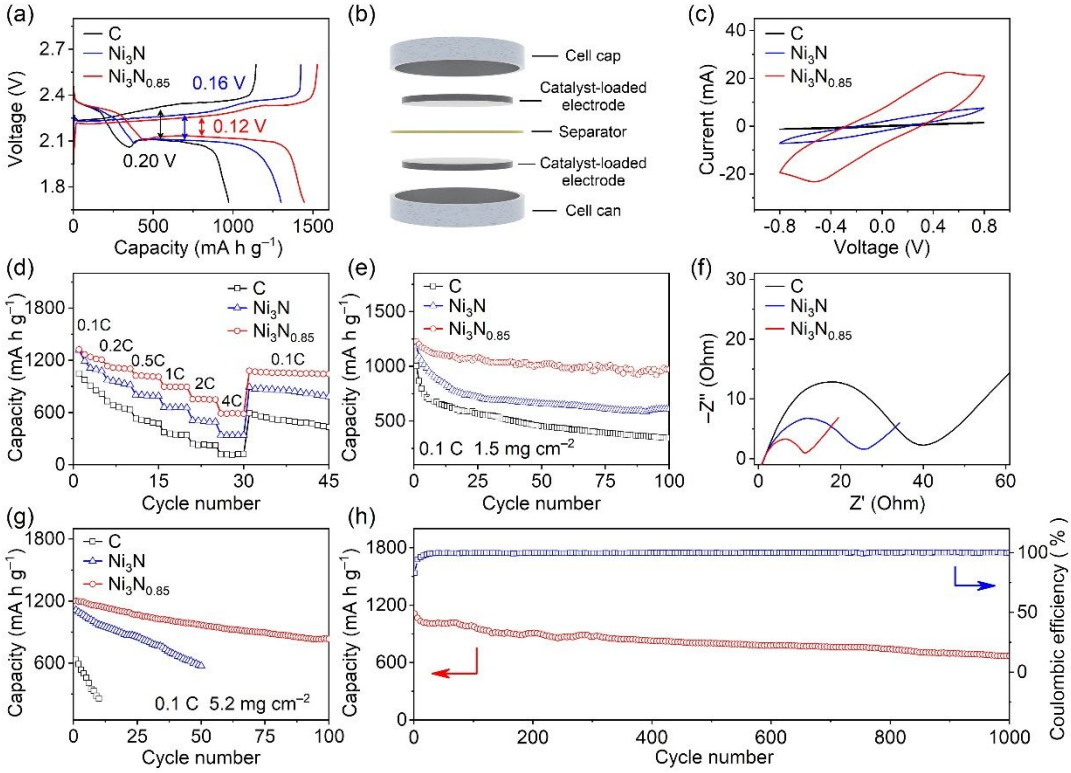

Figure 5. Electrochemical performances of C, Ni_3N, and $Ni_3N_{0.85}$ cathodes: (a) Galvanostatic discharge-charge

profiles at 0.02 C with the S loading of 1.5 mg cm^{-2}. (b) Schematic illustration of a symmetric cell configuration. (c) CV curves of symmetric cells using different S hosts (C, Ni_3N, and $Ni_3N_{0.85}$) and Li_2S_4-containing electrolyte. (d) Rate performance of the three cathodes at varied current densities. (e) Capacity retention of the three cathodes at 0.1 C for 100 cycles. (f) Nyquist plot of the three cathodes after 10 cycles at 0.1 C. (g) Cycling properties at a high S loading of 5.2 mg cm^{-2}. (h) Long-term cycling test of the $Ni_3N_{0.85}$ cathode.

To study what influence $Ni_3N_{0.85}$ has on anodes of Li-S batteries, we disassembled three cycled cells that used C, Ni_3N, and $Ni_3N_{0.85}$ as the cathodes and studied the morphologic and elemental changes of their Li anodes. Figure 6a-c present the SEM images of three Li anodes. The Li anode of the C cell shows rough and porous surfaces. Dendrite and solid Li can also be observed along the porous regions. The EDX plot in Figure 6d indicates that a large amount of S appears on the surface, implying the polysulfide migration from the S cathode to the Li anode. The rough surface may result from the deposited S modulating the growth morphology of Li. In contrast, the Li anodes of the cells using Ni_3N and $Ni_3N_{0.85}$ show relatively flat surface morphology. A simple comparison of EDX plots in Figure 6e,f allows one to see that S species had been significantly reduced on the anode of the $Ni_3N_{0.85}$ cell. A reduced polysulfide migration may lead to the relatively flat anode surface, which helps to form relatively stable SEI and contribute to the cyclability improvement. The cross-sectional SEM images in Figure S15 further confirm that the cycled Li in the $Ni_3N_{0.85}$ cell has more flat surface and less corrosion than the other two cells, indicative of the suppressed polysulfides migration.[44-46] These post-mortem analyses may allow us to conclude that N vacancies enhance the interaction between polysulfides and catalysts and accelerate their conversion, relatively suppressing the polysulfide migration.

Although we demonstrated the *d*-band tuning strategy with N vacancies here, there are still many other approaches to adjusting the electronic structures of catalysts to accelerate polysulfide conversion, for example, cation substitution or anion doping, selectively exposed surface, heterostructure construction. In addition, *p*-band interactions can also be used to tweak the catalysis activities. By modulating the electronic structures, Li-S batteries chemistry can be understood well at molecular or atomic scales. Given that polysulfides have a relatively large diversity of geometries, conductivity, polarity, and solubility, we must admit that one strategy can improve the performance, but may not shoot all issues. Therefore, other strategies like polysulfide confinement, conductive network, blocking separator, adsorbents should be combined to further improve the issues of Li-S batteries from atom to electrode levels.

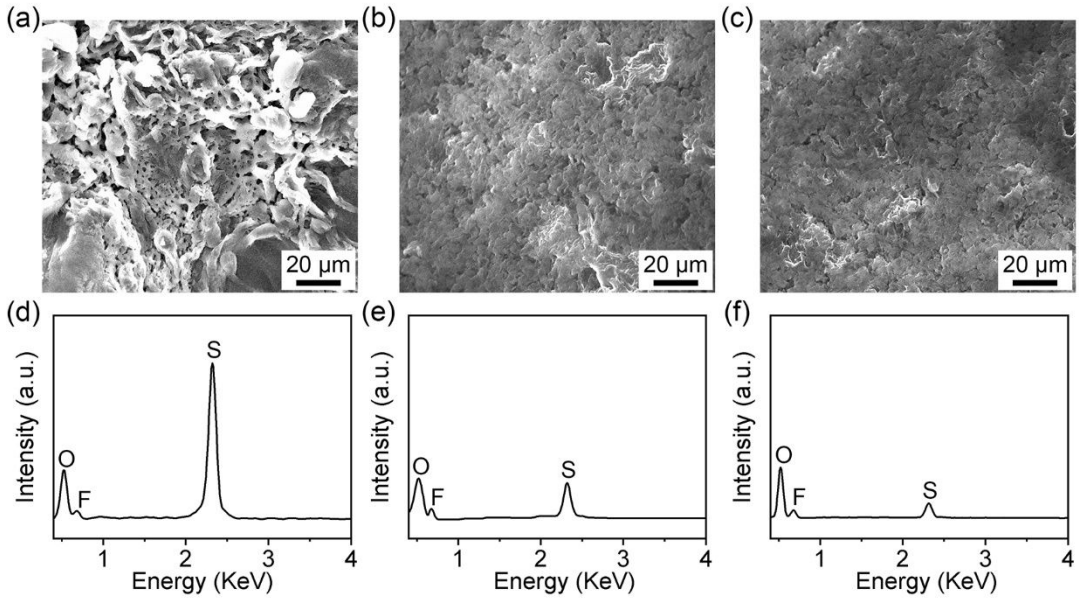

Figure 6. Post-mortem analysis of cycled Li-S battery anodes: SEM images of the cycled Li anodes that were assembled with the cathodes of (a) C, (b) Ni_3N, and (c) $Ni_3N_{0.85}$, respectively. (d-f) Corresponding EDX plots of the cycled Li anodes: (d) C, (e) Ni_3N, and (f) $Ni_3N_{0.85}$.

CONCLUSIONS

In summary, we proposed N vacancy-engineered $Ni_3N_{0.85}$ for efficiently catalyzing the conversion of polysulfides. The overall strategy is to adjust the *d*-band of Ni_3N rationally by introducing N vacancies. The upshift of *d*-band centers renders surface Ni bridging sites strongly adsorbing the terminal S atoms and weakening the S-S bonds. The temperature-dependent experiments demonstrated that $Ni_3N_{0.85}$ has much lower activation energy than Ni_3N and C. After assembled into Li-S batteries, $Ni_3N_{0.85}$ significantly promoted the polysulfide conversion and improved the electrochemical properties of batteries. Because of the enhanced kinetics, the overall cycling properties were also improved. A $Ni_3N_{0.85}$ cell can deliver a high capacity of 1200.4 mAh g^{-1} with a loading of 5.2 mg cm^{-2}. Even after 1000 cycles, the $Ni_3N_{0.85}$ cell can still show 61% capacity retentions. We believe that $Ni_3N_{0.85}$ materials and the *d*-band tuning strategy for accelerated catalysis will advance the development of high-performance Li-S batteries.

EXPERIMENTAL

Synthesis of hollow $Ni_3N_{0.85}$ nanocubes: Cu_2O templates were prepared according to the references.[47] The obtained prepared Cu_2O (0.1 g) was added into an ethanol-water mixed solvent (100 mL, volume ratio = 1:1) containing $NiCl_2{\cdot}6H_2O$ (0.034 g) and polyvinylpyrrolidone (MW = 30000, 3.33 g). After stirring for 1 h, 40 mL $Na_2S_2O_3$ aqueous solution (1 M) was added into the suspension until its color changed from red to green-yellow. The precipitates were rinsed and centrifuged several times with deionized water and absolute ethanol. The resulting hollow $Ni(OH)_2$ nanocubes were then annealed in an NH_3 atmosphere at 300 °C for 120 min to yield Ni_3N nanocubes. The N vacancies can be adjusted by varying the treatment time or temperature in Ar/H_2. The vacancies ratio can be adjusted in the range of x <= 0.15 by varying the treatment times under Ar/H_2 (Table S5). A longer time or more reducing atmosphere leads to the formation of metallic nickel. Table S5

presents the preparation conditions for samples with different Ni:N ratios. Figure S16 shows that the $Ni_3N_{0.85}$ sample has the highest catalytic activity.

Synthesis of $Ni_3N_{0.85}$, Ni_3N, and C cathodes: The S loading was conducted *via* a conventional melt-diffusion approach according to previous reports.[1, 11] S was mixed with $Ni_3N_{0.85}$, Ni_3N, and C and then heated at 155 °C in a sealed container for 6 h under Ar gas. As super-P was used in the batteries of $Ni_3N_{0.85}$ and Ni_3N, a C sample (pure super-P) was also prepared for comparison and to exclude the influence of super-P when characterizing the catalytic performance.

Polysulfide adsorption test: S and Li_2S with a molar ratio of 3:1 were added to an appropriate amount of 1, 2-dimethoxyethane (DME) and 1, 3-dioxolane (DOL) under vigorously magnetic stirring at 50 °C to prepare 0.5 mol L^{-1} Li_2S_4 solutions. After fully dissolved, an equivalent amount (50 mg) of C, Ni_3N, and $Ni_3N_{0.85}$ were immersed into 5 mL of the as-prepared Li_2S_4 solution, respectively. Optical images were compared to show the difference in adsorption capability at different times.

Reaction kinetics: Approximately 80 wt% catalysts (Ni_3N or $Ni_3N_{0.85}$) was mixed with 10 wt% super-P and 10 wt% polyvinylidene fluoride (PVDF) in N-methy-2-pyrrolidone (NMP) to form a slurry, which was then cast on Al foil. The loading of catalysts was ~2 mg cm^{-2}. Li foil and Celgard 2300 membranes were used as the anode and separator, respectively. For Li_2S nucleation tests, a tetraglyme solution containing 0.3 mol L^{-1} Li_2S_8 and 1.0 mol L^{-1} lithium bis(trifluoromethanesulfonyl)imide (LiTFSI) was used as catholyte. Li_2S_8 catholyte (20 μL) was dropped onto the cast C, Ni_3N, or $Ni_3N_{0.85}$ electrodes while 20 μL blank electrolyte without Li_2S_8 was added in the anode compartment. The assembled cells were galvanostatically discharged at 0.1 mA to 2.06 V and then maintained the voltage at 2.05 V to make Li_2S nucleate and grow. The potentiostatic discharge

was stopped after about 65000 s. For symmetric cells, the electrolyte containing about 0.5 M Li_2S_4 and 1 M LiTFSI was prepared in DME and DOL (1:1, V:V) solution. The obtained electrodes were used as cathode and anode. CV measurements of these symmetric cells were conducted between -0.8 and 0.8 V at a scan rate of 50 mV s^{-1}.

Electrochemical measurements: Three typical S cathodes were prepared by mixing active materials (C, Ni_3N, or $Ni_3N_{0.85}$ cathodes), Super P, and PVDF in NMP. The ratio of active materials, super-P, and PVDF was 8:1:1 and the sulfur loading is 1.5 mg cm^{-2} or 5.2 mg cm^{-2}. The resulting slurry was casted on the Al foil and dried at 60 °C overnight under vacuum. Coin cells were assembled in an Ar-filled glovebox with Celgard 2300 membrane and Li metal as the separator and anode, respectively. A 1 M LiTFSI solution in 1:1 (V:V) mixture of DME and DOL with 1% $LiNO_3$ was used as an electrolyte. The electrolyte used is controlled to be 50 μL. The cross-sectional SEM images of samples were presented in Figure S17. For temperature-dependent measurements, the coin cells were placed in a furnace. The temperatures were hold at 30, 40, and 50 °C, respectively. Two metallic wires were connected to Li–S batteries and led out to the potentiostat. CV curves were scanned at 0.1 mV s^{-1}. Those cells were galvanostatically charged and discharged using a Land Battery Tester (Lanhe, China). CV studies were carried out with a potentiostat (Bio-Logic, France).

Materials characterizations: XRD patterns were collected on a Rigaku D/MAX2500V with Cu Kα radiation (λ = 1.5418 Å). SEM images and EDX spectra were obtained with a Zeiss Ultra 55 field-emission gun SEM. XPS was recorded on an ESCALab MKII X-ray photoelectron spectrometer with nonmonochromatized Mg Kα X-ray as the excitation source. The binding energies in XPS analysis were corrected by referencing C 1s to 284.6 eV.

First Principle Calculation: Polysulfides adsorption was modeled in the framework of DFT using a CASTEP code.[48] The exchange-correlation functional used is the Perdew-Burke-Ernzerhof (PBE) of generalized gradient approximation (GGA).[49, 50] A plane wave cut-off energy of 550 eV is adopted for the standard norm-conserving pseudopotentials. Custom k-point grids of 5×5×2 and 3×3×1 were used for bulk Ni_3N material and all surface structures, respectively. The binding energy (E_b) between the substrate and polysulfides was calculated as follows:

$$E_b = E_{S+sub} - E_S - E_{sub}$$

Where E_S, E_{sub}, and E_{S+sub} are the energy of polysulfides, substrate, and polysulfides-substrate. The COOP was calculated using LOBSTER 3.2.0 code.[51-54] Wannier orbitals were obtained using a Wannier90 program.[55]

ASSOCIATED CONTENT

The Supporting Information is available free of charge *via* the Internet at http://pubs.acs.org."

Electron density differences of Ni_3N_{1-x}; Bader charge analysis; crystal structures and Ni-Ni bond length; geometric configurations and binding energies of polysulfides on Ni_3N and $Ni_3N_{0.85}$; visualized adsorption of Li_2S_4; optimized structures and bond length changes; SEM, TEM and nitrogen adsorption isotherms; TEM image and EDX scan; XPS spectra of S 2p; CV curves and Nyquist plots; SEM and TEM images of Ni_3N nanocubes; XRD pattern of $Ni_3N_{0.85}$-S cathode after cycling; comparison of reported metal nitrides; cross-section SEM images of lithium anodes after cycling; summary of chemical compositions analyzed by ICP-OES; EIS spectra and CV curves of symmetric cells; cross-section SEM images of $Ni_3N_{0.85}$-S composites with

varied S loading (PDF)

The authors declare no competing financial interest.

AUTHOR INFORMATION

Corresponding Author

*Prof. H. Zhang, hgzhang@nju.edu.cn

*Dr. J. Lu, junlu@anl.gov

ACKNOWLEDGMENT

The authors acknowledge the financial support of the National Natural Science Foundation of China (21776121), National Key Research and Development Program of China (No. 2017YFA0205700). The work at Argonne National Laboratory was supported by the U. S. Department of Energy (DOE), Office of Energy Efficiency and Renewable Energy, Vehicle Technologies Office. Argonne National Laboratory is operated for DOE Office of Science by UChicago Argonne, LLC, under contract number DE-AC02-06CH11357. The numerical calculations in this paper have been done on the computing facilities in the High-Performance Computing Center (HPCC) of Nanjing University.

REFERENCES

1. Wu, F.; Chen, S.; Srot, V.; Huang, Y.; Sinha, S. K.; Van Aken, P. A.; Maier, J.; Yu, Y. A Sulfur-Limonene-Based Electrode for Lithium-Sulfur Batteries: High-Performance by Self-Protection. *Adv. Mater.* **2018,** *30,* 1706643.

2. Wu, W.; Pu, J.; Wang, J.; Shen, Z.; Tang, H.; Deng, Z.; Tao, X.; Pan, F.; Zhang, H. Biomimetic Bipolar

Microcapsules Derived from *Staphylococcus Aureus* for Enhanced Properties of Lithium-Sulfur Battery Cathodes. *Adv. Energy Mater.* **2018,** *8,* 1702373.

3. Chung, S.-H.; Manthiram, A. Current Status and Future Prospects of Metal-Sulfur Batteries. *Adv. Mater.* **2019,** *31,* 1901125.

4. Fan, L.; Li, M.; Li, X.; Xiao, W.; Chen, Z.; Lu, J. Interlayer Material Selection for Lithium-Sulfur Batteries. *Joule* **2019,** *3,* 361–386.

5. Yan, Y.; Cheng, C.; Zhang, L.; Li, Y.; Lu, J. Deciphering the Reaction Mechanism of Lithium-Sulfur Batteries by *In Situ*/*Operando* Synchrotron-Based Characterization Techniques. *Adv. Energy Mater.* **2019,** *9,* 1900148.

6. Kou, W.; Li, X.; Liu, Y.; Zhang, X.; Yang, S.; Jiang, X.; He, G.; Dai, Y.; Zheng, W.; Yu, G. Triple-Layered Carbon-SiO_2 Composite Membrane for High Energy Density and Long Cycling Li-S Batteries. *ACS Nano* **2019,** *13,* 5900–5909.

7. Shen, S.; Xia, X.; Zhong, Y.; Deng, S.; Xie, D.; Liu, B.; Zhang, Y.; Pan, G.; Wang, X.; Tu, J. Implanting Niobium Carbide into Trichoderma Spore Carbon: A New Advanced Host for Sulfur Cathodes. *Adv. Mater.* **2019,** *31,* 1900009.

8. Xiao, Z.; Yang, Z.; Li, Z.; Li, P.; Wang, R. Synchronous Gains of Areal and Volumetric Capacities in Lithium-Sulfur Batteries Promised by Flower-Like Porous $Ti_3C_2T_x$ Matrix. *ACS Nano* **2019,** *13,* 3404–3412.

9. Chen, Y.; Zhang, W.; Zhou, D.; Tian, H.; Su, D.; Wang, C.; Stockdale, D.; Kang, F.; Li, B.; Wang, G. Co-Fe Mixed Metal Phosphide Nanocubes with Highly Interconnected-Pore Architecture as an Efficient Polysulfide Mediator for Lithium-Sulfur Batteries. *ACS Nano* **2019,** *13,* 4731–4741.

10. Pu, J.; Shen, Z.; Zheng, J.; Wu, W.; Zhu, C.; Zhou, Q.; Zhang, H.; Pan, F. Multifunctional Co_3S_4@Sulfur Nanotubes for Enhanced Lithium-Sulfur Battery Performance. *Nano Energy* **2017,** *37,* 7–14.

11. Yu, Q.; Lu, Y.; Luo, R.; Liu, X.; Huo, K.; Kim, J.-K.; He, J.; Luo, Y. *In Situ* Formation of Copper-Based Hosts Embedded within 3D N-Doped Hierarchically Porous Carbon Networks for Ultralong Cycle Lithium-Sulfur Batteries. *Adv. Funct. Mater.* **2018,** *28,* 1804520.

12. Yuan, Y.; Lu, J. Demanding Energy from Carbon. *Carbon Energy* **2019,** *1,* 8–12.

13. Jiao, L.; Zhang, C.; Geng, C.; Wu, S.; Li, H.; Lv, W.; Tao, Y.; Chen, Z.; Zhou, G.; Li, J.; Ling, G.; Wan, Y.; Yang, Q.-H. Capture and Catalytic Conversion of Polysulfides by *In Situ* Built TiO_2-MXene Heterostructures for Lithium-Sulfur Batteries. *Adv. Energy Mater.* **2019,** *9,* 1900219.

14. Yang, X.; Gao, X.; Sun, Q.; Jand, S. P.; Yu, Y.; Zhao, Y.; Li, X.; Adair, K.; Kuo, L.-Y.; Rohrer, J.; Liang, J.; Lin, X.; Banis, M. N.; Hu, Y.; Zhang, H.; Li, X.; Li, R.; Zhang, H.; Kaghazchi, P.; Sham, T.-K., *et al.* Promoting the Transformation of Li_2S_2 to Li_2S: Significantly Increasing Utilization of Active Materials for High-Sulfur-Loading Li-S Batteries. *Adv. Mater.* **2019,** *31,* 1901220.

15. Zhang, Z.-W.; Peng, H.-J.; Zhao, M.; Huang, J.-Q. Heterogeneous/Homogeneous Mediators for High-Energy-Density Lithium-Sulfur Batteries: Progress and Prospects. *Adv. Funct. Mater.* **2018,** *28,* 1707536.

16. Babu, G.; Ababtain, K.; Simon Ng, K. Y.; Arava, L. M. R. Electrocatalysis of Lithium Polysulfides: Current Collectors as Electrodes in Li/S Battery Configuration. *Sci. Rep.* **2015,** *5,* 8763.

17. Zhao, Q.; Hu, X.; Zhang, K.; Zhang, N.; Hu, Y.; Chen, J. Sulfur Nanodots Electrodeposited on Ni Foam as High-Performance Cathode for Li-S Batteries. *Nano Lett.* **2015,** *15,* 721–726.

18. Liu, Y.-T.; Han, D.-D.; Wang, L.; Li, G.-R.; Liu, S.; Gao, X.-P. $NiCo_2O_4$ Nanofibers as Carbon-Free Sulfur

Immobilizer to Fabricate Sulfur-Based Composite with High Volumetric Capacity for Lithium-Sulfur Battery. *Adv. Energy Mater.* **2019,** *9,* 1803477.

19. Wang, Y.; Zhang, R.; Chen, J.; Wu, H.; Lu, S.; Wang, K.; Li, H.; Harris, C. J.; Xi, K.; Kumar, R. V.; Ding, S. Enhancing Catalytic Activity of Titanium Oxide in Lithium–Sulfur Batteries by Band Engineering. *Adv. Energy Mater.* **2019,** *9,* 1900953.

20. Wang, Z.-Y.; Wang, L.; Liu, S.; Li, G.-R.; Gao, X.-P. Conductive CoOOH as Carbon-Free Sulfur Immobilizer to Fabricate Sulfur–Based Composite for Lithium-Sulfur Battery. *Adv. Funct. Mater.* **2019,** *29,* 1901051.

21. Wang, N.; Chen, B.; Qin, K.; Liu, E.; Shi, C.; He, C.; Zhao, N. Rational Design of Co_9S_8/CoO Heterostructures with Well-Defined Interfaces for Lithium Sulfur Batteries: A Study of Synergistic Adsorption-Electrocatalysis Function. *Nano Energy* **2019,** *60,* 332–339.

22. Shin, W.; Lu, J.; Ji, X. ZnS Coating of Cathode Facilitates Lean-Electrolyte Li-S Batteries. *Carbon Energy* **2019,** *1,* 165–172.

23. Wang, Z.; Shen, J.; Liu, J.; Xu, X.; Liu, Z.; Hu, R.; Yang, L.; Feng, Y.; Liu, J.; Shi, Z.; Ouyang, L.; Yu, Y.; Zhu, M. Self-Supported and Flexible Sulfur Cathode Enabled *via* Synergistic Confinement for High-Energy-Density Lithium-Sulfur Batteries. *Adv. Mater.* **2019,** *31,* 1902228.

24. Luo, L.; Chung, S.-H.; Asl, H. Y.; Manthiram, A. Long-Life Lithium-Sulfur Batteries with a Bifunctional Cathode Substrate Configured with Boron Carbide Nanowires. *Adv. Mater.* **2018,** *30,* 1804149.

25. Hao, B.; Li, H.; Lv, W.; Zhang, Y.; Niu, S.; Qi, Q.; Xiao, S.; Li, J.; Kang, F.; Yang, Q.-H. Reviving Catalytic Activity of Nitrides by the Doping of the Inert Surface Layer to Promote Polysulfide Conversion in Lithium-

Sulfur Batteries. *Nano Energy* **2019,** *60,* 305–311.

26. Zhao, M.; Peng, H.-J.; Zhang, Z.-W.; Li, B.-Q.; Chen, X.; Xie, J.; Chen, X.; Wei, J.-Y.; Zhang, Q.; Huang, J.-Q. Activating Inert Metallic Compounds for High-Rate Lithium-Sulfur Batteries through *In Situ* Etching of Extrinsic Metal. *Angew. Chem. Int. Ed.* **2019,** *58,* 3779–3783.

27. Zhong, Y.; Chao, D.; Deng, S.; Zhan, J.; Fang, R.; Xia, Y.; Wang, Y.; Wang, X.; Xia, X.; Tu, J. Confining Sulfur in Integrated Composite Scaffold with Highly Porous Carbon Fibers/Vanadium Nitride Arrays for High-Performance Lithium-Sulfur Batteries. *Adv. Funct. Mater.* **2018,** *28,* 1706391.

28. Zhou, J.; Liu, X.; Zhu, L.; Zhou, J.; Guan, Y.; Chen, L.; Niu, S.; Cai, J.; Sun, D.; Zhu, Y.; Du, J.; Wang, G.; Qian, Y. Deciphering the Modulation Essence of p Bands in Co-Based Compounds on Li-S Chemistry. *Joule* **2018,** *2,* 2681–2693.

29. Li, B.-Q.; Kong, L.; Zhao, C.-X.; Jin, Q.; Chen, X.; Peng, H.-J.; Qin, J.-L.; Chen, J.-X.; Yuan, H.; Zhang, Q.; Huang, J.-Q. Expediting Redox Kinetics of Sulfur Species by Atomic-Scale Electrocatalysts in Lithium-Sulfur Batteries. *InfoMat* **2019,** *1,* 533–541.

30. Shen, Z.; Cao, M.; Zhang, Z.; Pu, J.; Zhong, C.; Li, J.; Ma, H.; Li, F.; Zhu, J.; Pan, F.; Zhang, H. Efficient $Ni_2Co_4P_3$ Nanowires Catalysts Enhance Ultrahigh-Loading Lithium-Sulfur Conversion in a Microreactor-Like Battery. *Adv. Funct. Mater.* **2020,** *30,* 1906661.

31. Li, N.; Su, D. *In-Situ* Structural Characterizations of Electrochemical Intercalation of Graphite Compounds. *Carbon Energy* **2019,** *1,* 200–218.

32. Hammer, B.; Norskov, J. K. Theoretical Surface Science and Catalysis Calculations and Concepts. *Adv. Catal.* **2000,** *45,* 71–129.

33. Fan, F. Y.; Craig Carter, W.; Chiang, Y.-M. Mechanism and Kinetics of Li_2S Precipitation in Lithium-Sulfur Batteries. *Adv. Mater.* **2015,** *27,* 5203–5209.

34. Li, Q.; Zou, X.; Ai, X.; Chen, H.; Sun, L.; Zou, X. Revealing Activity Trends of Metal Diborides toward pH-Universal Hydrogen Evolution Electrocatalysts with Pt-Like Activity. *Adv. Energy Mater.* **2018,** *9,* 1803369.

35. Yuan, H.; Huang, J.-Q.; Peng, H.-J.; Titirici, M.-M.; Xiang, R.; Chen, R.; Liu, Q.; Zhang, Q. A Review of Functional Binders in Lithium-Sulfur Batteries. *Adv. Energy Mater.* **2018,** *8,* 1802107.

36. Xu, K.; Chen, P.; Li, X.; Tong, Y.; Ding, H.; Wu, X.; Chu, W.; Peng, Z.; Wu, C.; Xie, Y. Metallic Nickel Nitride Nanosheets Realizing Enhanced Electrochemical Water Oxidation. *J. Am. Chem. Soc.* **2015,** *137,* 4119–4125.

37. Dhunna, R.; Lal, C.; Avasthi, D. K.; Barman, S. R.; Ganesan, V.; Jain, I. P. Irradiation Induced Effects on Ni_3N/Si Bilayer System. *Vacuum* **2009,** *83,* 1448–1453.

38. Wang, Y.; Fu, Z.-W.; Yue, X.-L.; Qin, Q.-Z. Electrochemical Reactivity Mechanism of Ni_3N with Lithium. *J. Electrochem. Soc.* **2004,** *151,* E162–E167.

39. Liu, B.; He, B.; Peng, H.-Q.; Zhao, Y.; Cheng, J.; Xia, J.; Shen, J.; Ng, T.-W.; Meng, X.; Lee, C.-S.; Zhang, W. Unconventional Nickel Nitride Enriched with Nitrogen Vacancies as a High-Efficiency Electrocatalyst for Hydrogen Evolution. *Adv. Sci.* **2018,** *5,* 1800406.

40. Xia, B.; Wang, T.; Chi, X.; Yu, X.; Liu, P.; Zhang, J.; Xi, S.; Du, Y.; Gao, D. Anion Vacancy-Mediated Ferromagnetism in Atomic-Thick Ni_3N Nanosheets. *Appl. Phys. Lett.* **2017,** *111,* 232402.

41. Liang, X.; Kwok, C. Y.; Lodi-Marzano, F.; Pang, Q.; Cuisinier, M.; Huang, H.; Hart, C. J.; Houtarde, D.; Kaup, K.; Sommer, H.; Brezesinski, T.; Janek, J.; Nazar, L. F. Tuning Transition Metal Oxide-Sulfur

Interactions for Long Life Lithium Sulfur Batteries: The “Goldilocks” Principle. *Adv. Energy Mater.* **2016,** *6,* 1501636.

42. Yao, Y.; Wang, H.; Yang, H.; Zeng, S.; Xu, R.; Liu, F.; Shi, P.; Feng, Y.; Wang, K.; Yang, W.; Wu, X.; Luo, W.; Yu, Y. A Dual-Functional Conductive Framework Embedded with TiN-VN Heterostructures for Highly Efficient Polysulfide and Lithium Regulation toward Stable Li-S Full Batteries. *Adv. Mater.* **2019,** *32,* e1905658.

43. Wu, Q.; Zhou, X.; Xu, J.; Cao, F.; Li, C. Adenine Derivative Host with Interlaced 2D Structure and Dual Lithiophilic-Sulfiphilic Sites to Enable High-Loading Li-S Batteries. *ACS Nano* **2019,** *13,* 9520–9532.

44. Wu, F.; Lv, H.; Chen, S.; Lorger, S.; Srot, V.; Oschatz, M.; Van Aken, P. A.; Wu, X.; Maier, J.; Yu, Y. Natural Vermiculite Enables High-Performance in Lithium-Sulfur Batteries *via* Electrical Double Layer Effects. *Adv. Funct. Mater.* **2019,** *29,* 1902820.

45. Osella, S.; Minoia, A.; Quarti, C.; Cornil, J.; Lazzaroni, R.; Goffin, A. L.; Guillaume, M.; Beljonne, D. Modelling Coupled Ion Motion in Electrolyte Solutions for Lithium-Sulfur Batteries. Batteries Supercaps. 2019, 2, 473–481.

46. Gong, Y.; Fu, C.; Dong, A.; Zhou, H. Li, H.; Kuang, Y. Polar Ultrathin Self-Doping Carbon Nitride Nanosheets with Intrinsic Polysulfide Adsorption for High Performance Lithium-Sulfur Batteries. Batteries Supercaps. 2018, 1, 192–201.

47. Liang, H.; Gandi, A. N.; Anjum, D. H.; Wang, X.; Schwingenschlogl, U.; Alshareef, H. N. Plasma-Assisted Synthesis of NiCoP for Efficient Overall Water Splitting. *Nano Lett.* **2016,** *16,* 7718–7725.

48. Clark, S. J.; Segall, M. D.; Pickard, C. J.; Hasnip, P. J.; Probert, M. I. J.; Refson, K.; Payne, M. C. First Principles Methods Using CASTEP. *Z. Krist. Cryst. Mater.* **2005,** *220,* 567–570.

49. Grimme, S. Semiempirical GGA-Type Density Functional Constructed with a Long-Range Dispersion Correction. *J. Comput. Chem.* **2006,** *27,* 1787–1799.

50. Perdew, J. P.; Burke, K.; Ernzerhof, M. Generalized Gradient Approximation Made Simple. *Phys. Rev. Lett.* **1996,** *77,* 3865–3868.

51. Deringer, V. L.; Tchougreeff, A. L.; Dronskowski, R. Crystal Orbital Hamilton Population (COHP) Analysis as Projected from Plane-Wave Basis Sets. *J. Phys. Chem. A* **2011,** *115,* 5461–5466.

52. Dronskowski, R.; Blochl, P. E. Crystal Orbital Hamilton Populations (COHP) Energy-Resolved Visualization of Chemical Bonding in Solids Based on Density-Functional Calculations. *J. Phys. Chem.* **1993,** *97,* 8617–8624.

53. Maintz, S.; Deringer, V. L.; Tchougreeff, A. L.; Dronskowski, R. Analytic Projection from Plane-Wave and PAW Wavefunctions and Application to Chemical-Bonding Analysis in Solids. *J. Comput. Chem.* **2013,** *34,* 2557–2567.

54. Maintz, S.; Deringer, V. L.; Tchougreeff, A. L.; Dronskowski, R. LOBSTER: A Tool to Extract Chemical Bonding from Plane-Wave Based DFT. *J. Comput. Chem.* **2016,** *37,* 1030–1035.

55. Mostofi, A. A.; Yates, J. R.; Pizzi, G.; Lee, Y.-S.; Souza, I.; Vanderbilt, D.; Marzari, N. An Updated Version of Wannier90: A Tool for Obtaining Maximally-Localised Wannier Functions. *Comput. Phys. Commun.* **2014,** *185,* 2309–2310.

For Table of Contents Only

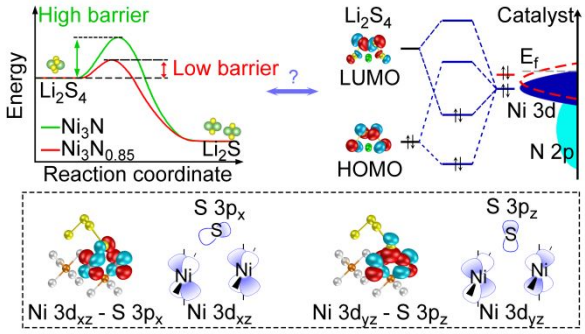

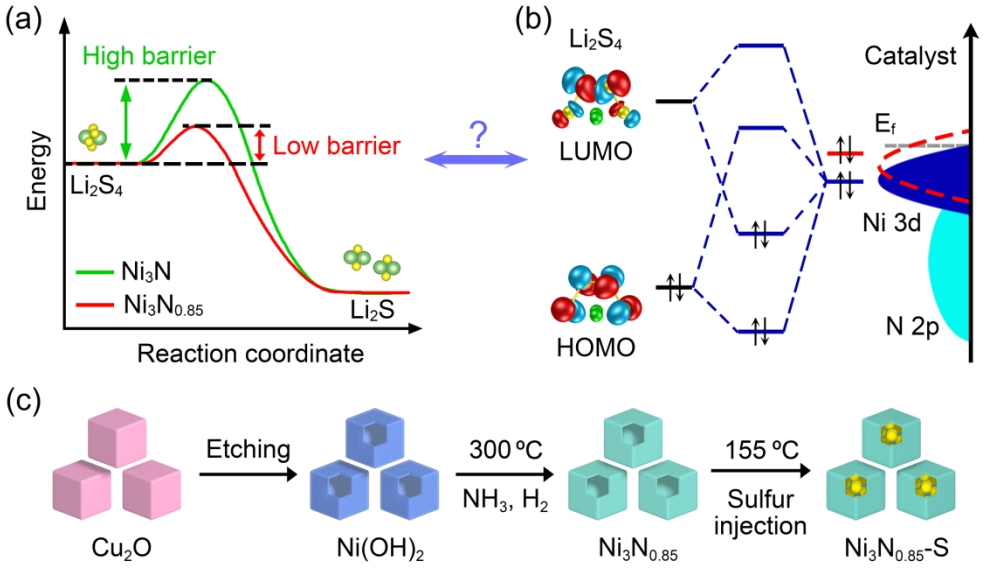

Figure 1. Schematic illustration of rational catalyst design by correlating (a) activation barrier with (b) orbital interactions between polysulfides and catalysts. Schematic diagram of the preparation procedures of Ni3N1−x−S cathodes.

117x69mm (600 x 600 DPI)

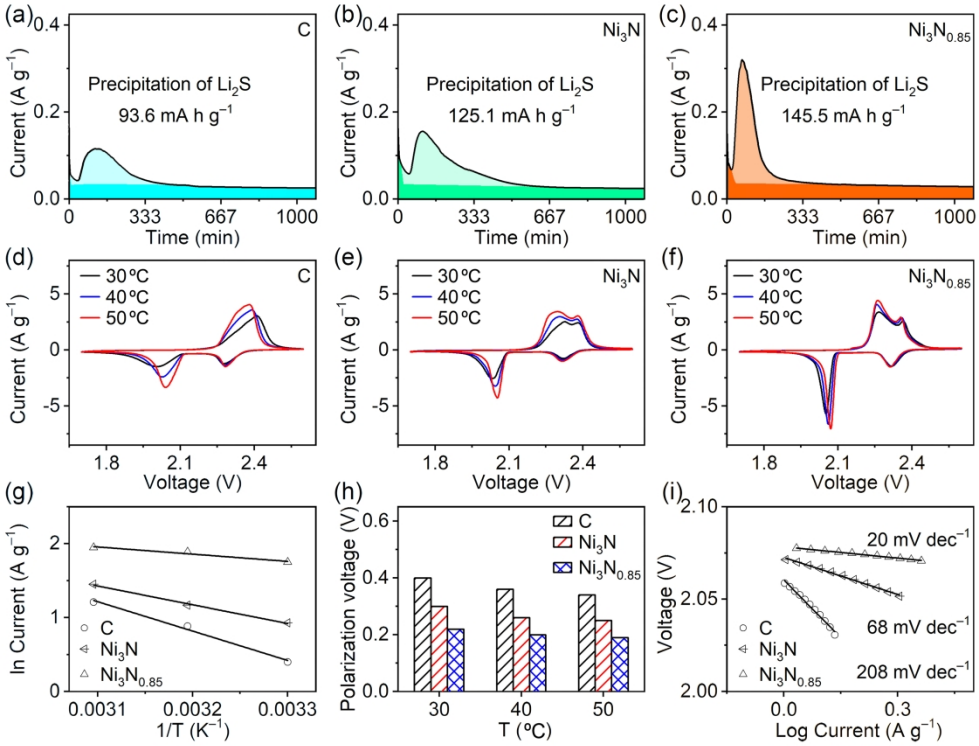

Figure 2. Electrochemical characterizations of electrocatalysts: (a–c) Chronoamperometric curves of nucleation tests using (a) C, (b) Ni3N, and (c) Ni3N0.85 in a Li2S8/tetraglyme solution at 2.05 V (the regions with light and dark colors indicate the precipitation of Li2S and the reduction of Li2S8/Li2S6, respectively). (d–f) CV curves of (d) C, (e) Ni3N, and (f) Ni3N0.85 at different temperatures. (g) Relation of Li2S4 conversion rates with respect to temperatures in Li-S cells using C, Ni3N, and Ni3N0.85. (h) Polarization voltage gaps of the reduction peaks around 2 V and their corresponding oxidation peaks. (i) Tafel plots for the CV curves between 2.03 and 2.08 V at 30 °C.

142x108mm (600 x 600 DPI)

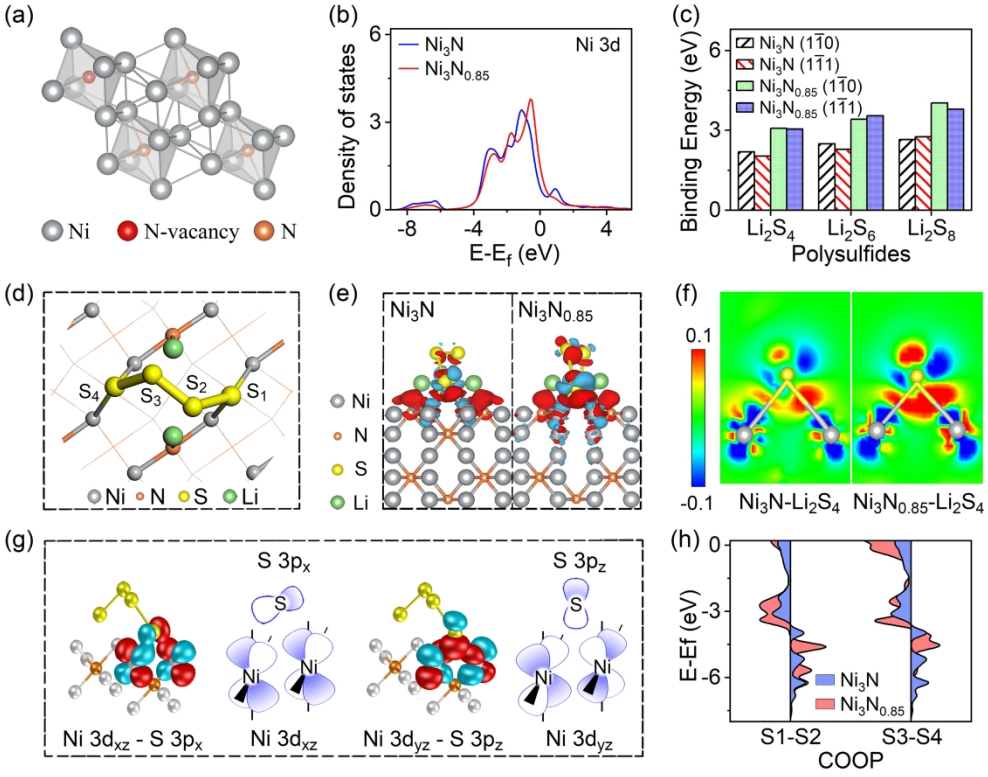

Figure 3. Theoretic analysis of the catalytic conversion of Li2S4: (a) Crystal structure of Ni3N0.85 for DFT calculations. (b) Partial density of states for Ni 3d orbitals of Ni3N and Ni3N0.85. (c) Calculated binding energies between LiPSs (Li2S4, Li2S6, Li2S8) and catalysts (Ni3N or Ni3N0.85). (d) Optimized configuration of Li2S4 on Ni3N0.85. (e) Electron density differences of Li2S4 on Ni3N and Ni3N0.85 (the red and cyan regions represent negative and positive change the isovalue of ± 0.05). (f) Electron density differences in the slice planes through Ni-S-Ni bonds. (g) Interaction diagram of Wannier orbitals of Li2S4 on Ni3N. (h) COOP diagram of the S1-S2 and S3-S4 bonds of Li2S4-absorbed Ni3N and Ni3N0.85.

142x112mm (600 x 600 DPI)

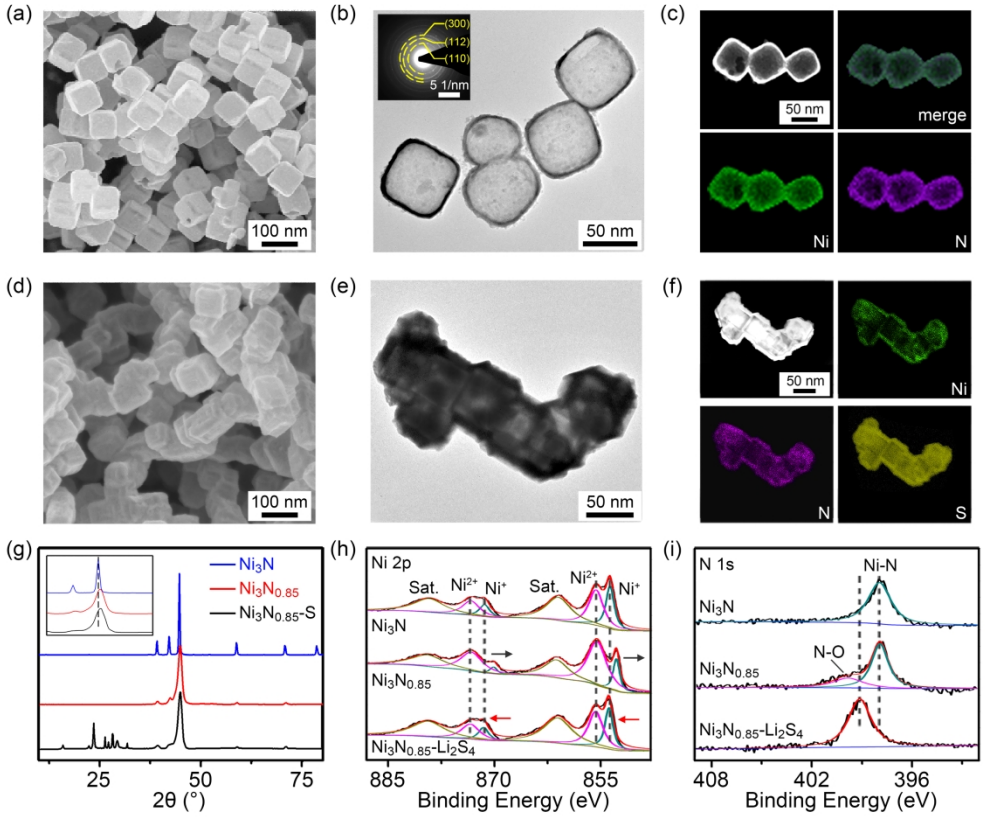

Figure 4. Materials characterizations of electrocatalysts: (a) SEM and (b) TEM images of as-prepared Ni3N0.85 nanocubes (the inset in (b) is the SAED pattern of nanocube). (c) STEM image and EDX mapping images of el-emental Ni and N in Ni3N0.85 nanocubes. (d) SEM, (e) TEM, and (f) EDX elemental mapping images of Ni3N0.85–S nanocubes. (g) XRD patterns of Ni3N, Ni3N0.85, and Ni3N.085–S (the inset shows the zoomed region of (111) peaks). XPS spectra of (h) Ni 2p and (i) N 1s for Ni3N, Ni3N0.85, and Ni3N0.85–Li2S4.

142x119mm (600 x 600 DPI)

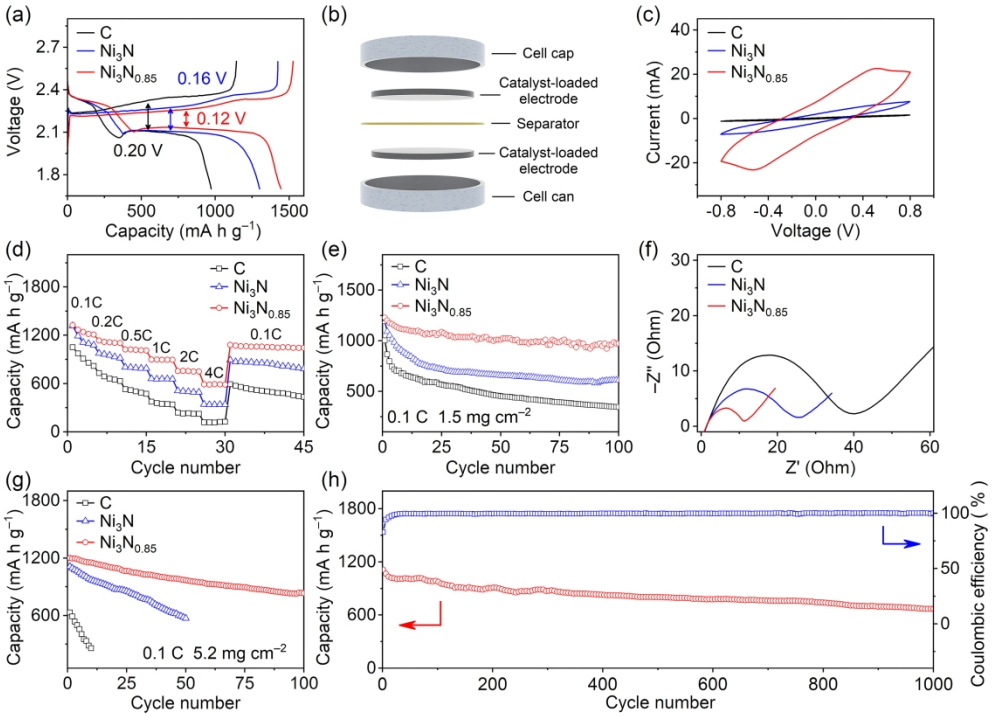

Figure 5. Electrochemical performances of C, Ni3N, and Ni3N0.85 cathodes: (a) Galvanostatic discharge-charge profiles at 0.02 C with the S loading of 1.5 mg cm−2. (b) Schematic illustration of a symmetric cell configuration. (c) CV curves of symmetric cells using different S hosts (C, Ni3N, and Ni3N0.85) and Li2S4-containing electrolyte. (d) Rate performance of the three cathodes at varied current densities. (e) Capacity retention of the three cathodes at 0.1 C for 100 cycles. (f) Nyquist plot of the three cathodes after 10 cycles at 0.1 C. (g) Cycling properties at a high S loading of 5.2 mg cm−2. (h) Long-term cycling test of the Ni3N0.85 cathode.

142x102mm (600 x 600 DPI)

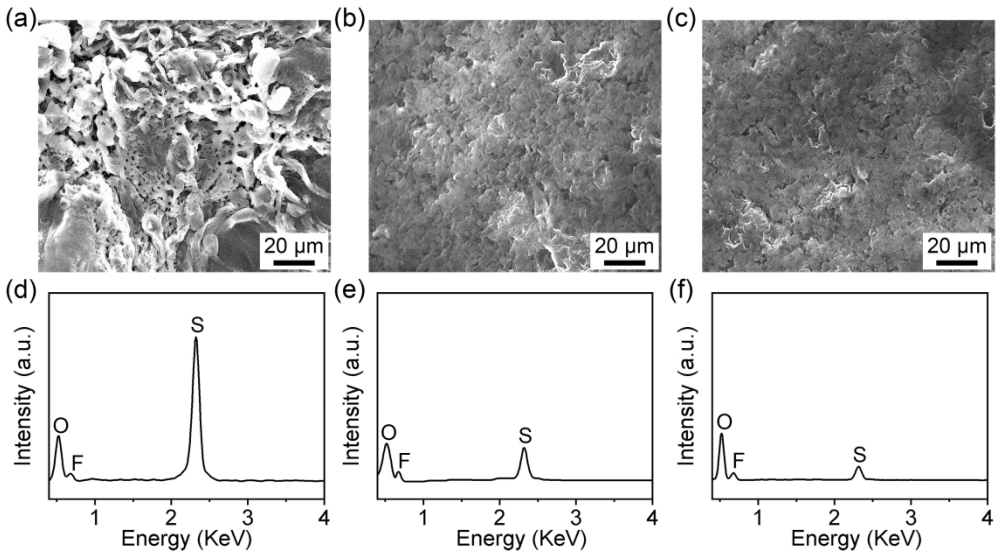

Figure 6. Post-mortem analysis of cycled Li-S battery anodes: SEM images of the cycled Li anodes that were assembled with the cathodes of (a) C, (b) Ni3N, and (c) Ni3N0.85, respectively. (d-f) Corresponding EDX plots of the cycled Li anodes: (d) C, (e) Ni3N, and (f) Ni3N0.85.

142x80mm (600 x 600 DPI)